Check for updates

*Small*

NANO · MICRO small
www.small-journal.com

RESEARCH ARTICLE OPEN ACCESS

# Optically Driven AuCu Alloying in Single Nanoparticles Revealed by In Situ TEM

Francesca Scalerandi | Loriane Monin | Nathan J. Mowry | Wiebke Albrecht

LMPV-Sustainable Energy Materials Department, AMOLF, Amsterdam, The Netherlands

**Correspondence:** Wiebke Albrecht (w.albrecht@amolf.nl)

**Received:** 30 April 2026 | **Revised:** 11 September 2026 | **Accepted:** 18 September 2026

**Keywords:** bimetallic nanoparticles | composition control | in situ TEM | photothermal alloying

## ABSTRACT

AuCu alloys are versatile materials whose physical and optical properties can be finely tuned through composition, making precise control over the Au/Cu ratio highly desirable. Here, we demonstrate that pulsed laser excitation provides a promising route to dynamically drive and control alloy formation in single nanoparticles. We track the structural and compositional evolution of individual Au@$TiO_2$ core–shell nanorods under optical excitation in situ using transmission electron microscopy combined with picosecond pulsed laser illumination. Laser irradiation mobilizes copper-containing species from the carbon support, which migrate to the nanorod surface and alloy with gold to form a homogeneous AuCu alloy. The copper fraction can be tuned with laser fluence, reaching values above 80%, before the local temperature exceeds the threshold for copper sublimation and a gold-rich structure is partially restored. Time-resolved diffraction shows that the process is reversible but kinetically asymmetric: incorporation is rapid, while the slower evaporative removal allows the copper fraction to be tuned more finely on the return path. These results demonstrate that, under pulsed laser excitation, nanoparticle composition can be actively driven, observed, and frozen on demand at the single-particle level through control of laser fluence and illumination time.

## 1 | Introduction

Bimetallic nanoparticles offer a versatile platform for tuning functionality through compositional design. This tunability ultimately depends on atomic-scale structure. In such systems, catalytic, optical, and electronic properties are not dictated solely by the overall composition, but also by the local distribution of elements, their degree of ordering, and particle morphology [1–4]. Au–Cu nanoparticles represent a particularly instructive model system in this regard [5–7]. Across their phase space, they span ordered intermetallic compounds ($Au_3Cu$, AuCu, $AuCu_3$) and disordered solid solutions, with properties that change sensitively with composition and atomic arrangement [8, 9]. At the same time, Au–Cu is a practically relevant system: Au stabilizes Cu against oxidation, while Cu introduces chemical reactivity and modifies the electronic and plasmonic response away from that of pure Au. In this system, the dependence of functionality on local composition and ordering is especially pronounced. For example, in plasmonic Au–Cu alloys, tuning the relative Au/Cu content modifies the balance between interband and intraband excitations, thereby altering the distribution of hot carriers and the dominant chemical reaction pathways [10]. In this way, composition can switch the system between distinct catalytic regimes, highlighting the potential for composition to act as an active control parameter rather than a static design variable.

However, achieving controlled and homogeneous alloying in Au–Cu nanoparticles remains a fundamental challenge. Chemical synthesis provides control over the average Au–Cu composition via precursor ratios and reaction conditions, but the substantially different reduction potentials of $Au^{3+}$ and $Cu^{2+}$ mean that synchronizing their reduction requires careful tuning

This is an open access article under the terms of the Creative Commons Attribution License, which permits use, distribution and reproduction in any medium, provided the original work is properly cited.
© 2026 The Author(s). *Small* published by Wiley-VCH GmbH

of ligands, precursors and stoichiometry, and reproducibility remains sensitive to small variations in conditions [5]. Particle-to-particle variability in composition is also pronounced at the single-particle level: Prunier et al. showed that nanoparticles synthesized with widely different target compositions exhibited nearly identical, strongly Au-rich compositions, because gold nucleates preferentially regardless of the precursor ratio [11]. Post-synthesis thermal annealing can drive further mixing and ordering [12], but Au–Cu nanoparticles also exhibit a tendency toward Au surface segregation due to the lower surface energy of Au [8, 11]. Critically, all conventional approaches (chemical synthesis, physical deposition, and thermal annealing) set the composition at the moment of preparation and provide no route to continuously and reversibly adjust it during operation or characterization.

In this context, pulsed optical excitation presents a compelling route to access and dynamically control alloy states that are difficult or impossible to reach through conventional methods [13]. The rapid heating during a laser pulse, followed by ultrafast quenching in the surrounding medium, can kinetically trap transient compositional states before long-range diffusion and segregation processes fully develop [13–15]. The resulting alloy structure reflects a balance between thermodynamic driving forces and kinetic constraints. While thermodynamics determines whether mixing or segregation is energetically favored, the extreme heating and cooling rates associated with pulsed laser excitation can prevent the system from fully relaxing toward equilibrium [16, 17]. As a result, metastable alloy configurations can be retained that are inaccessible from equilibrium phase diagrams, even in multicomponent systems where elemental segregation would otherwise be expected [18]. Consequently, pulsed laser ablation in liquids and laser excitation of pre-synthesized colloidal heterostructures have been explored to produce solid-solution alloys spanning from binary systems to high-entropy alloys of five or more elements, including combinations such as Au–Cu that are difficult to mix homogeneously by wet-chemical routes [11, 13]. For example, rapid cooling has been shown to stabilize Au-Fe alloy phases beyond their equilibrium miscibility limits [16]. Similarly, nanosecond laser irradiation of Au@Pd, Au@Pt and Au@Pd@Pt heterostructures was shown to promote interdiffusion at elevated temperatures, producing metastable and homogeneous AuPd, AuPt and AuPdPt alloy nanospheres [19]. Beyond kinetic trapping, pulsed laser offers unmatched temporal control. It can be switched on and off with electronic precision down to the single-pulse level, far faster than the thermal inertia of any resistive heater. This means compositional changes can be initiated, modulated, and paused with a precision and speed that no thermal approach can match. Once the laser is switched off, the composition is kinetically stable at room temperature indefinitely, since diffusion coefficients at ambient conditions are negligibly small [12].

Despite the demonstrated power of pulsed laser-assisted alloying, dynamic insight into how the process unfolds at the single-particle level remains difficult to obtain. Closing this gap requires following the process in real time, with simultaneous structural and compositional information at the level of individual nanoparticles. In situ TEM has emerged as a powerful platform for exactly this kind of study under external stimuli. In situ thermal heating has been used to follow alloying and atomic redistribution in bimetallic core–shell nanoparticles and nanowires, revealing how interdiffusion proceeds, how composition and ordering evolve over time, and how surface segregation and intermediate phases shape the final structure [12, 20]. These studies make clear that real-time, single-particle observation is what turns alloying from an inferred outcome into a mechanistically understood process. Extending the same level of dynamic insight to pulsed laser excitation is therefore essential, because laser-driven alloying is mechanistically distinct from thermal annealing, proceeding through rapid heating–quenching cycles under strongly non-equilibrium conditions. Ultrafast electron microscopy (UTEM) has provided dynamic insight into material responses using stroboscopic pump–probe schemes to resolve reversible structural dynamics from the femtosecond to microsecond regime, including in gold and graphite thin films [21, 22]. However, these approaches are primarily optimized for reversible processes that return to their initial state between successive pump–probe cycles and are therefore less suited to studying continuously evolving, diffusion-limited transformations such as alloying under pulsed illumination. Following such cumulative, diffusion-limited transformations in situ has recently become practical with the maturation of dedicated optical in-coupling systems for TEM [23], but the dynamics of laser-driven alloying have so far not been followed in real time at the single-particle level.

Here we exploit a TEM equipped with a picosecond pulsed laser light in-coupling unit to follow the structural and compositional evolution of AuNR@$TiO_2$ core–shell nanorods under optical excitation in real time. We show that laser illumination drives the migration of copper-containing species from the carbon support film onto the nanorod surface, where they alloy with gold to form a homogeneous AuCu solid solution. The Cu fraction in the resulting alloy, quantified by energy-dispersive X-ray spectroscopy (EDX) and tracked through lattice parameter shifts measured by electron diffraction, can be tuned continuously by adjusting laser fluence, reaching above 80% Cu incorporation before copper sublimates at higher fluences, restoring the original gold structure. This approach demonstrates that the composition of an individual nanoparticle can be actively tuned and modified under optical excitation, providing direct access to intermediate, non-equilibrium alloy states that are not readily achievable through conventional synthesis routes. More broadly, these results establish a pathway toward dynamic, light-driven control of nanoparticle composition at the single-particle level, where functionality may be adjusted in situ through optical excitation conditions.

## 2 | Results and Discussion

### 2.1 | Copper Incorporation Under Laser Illumination

To investigate laser-induced alloying of gold nanoparticles with copper, we used Au nanorods coated with an amorphous titania shell (AuNR@$TiO_2$) as our model system. The $TiO_2$ shell serves a dual purpose: it is a widely used support material in heterogeneous catalysis, making AuNR@$TiO_2$ a practically relevant catalyst architecture, and the shell suppresses



16136829, 0, Downloaded from https://onlinelibrary.wiley.com/doi/10.1002/smll.75977 by Centrum Voor Wiskunde En Info (Cwi), Wiley Online Library on [10/11/2026]. See the Terms and Conditions (https://onlinelibrary.wiley.com/terms-and-conditions) on Wiley Online Library for rules of use; OA articles are governed by the applicable Creative Commons License

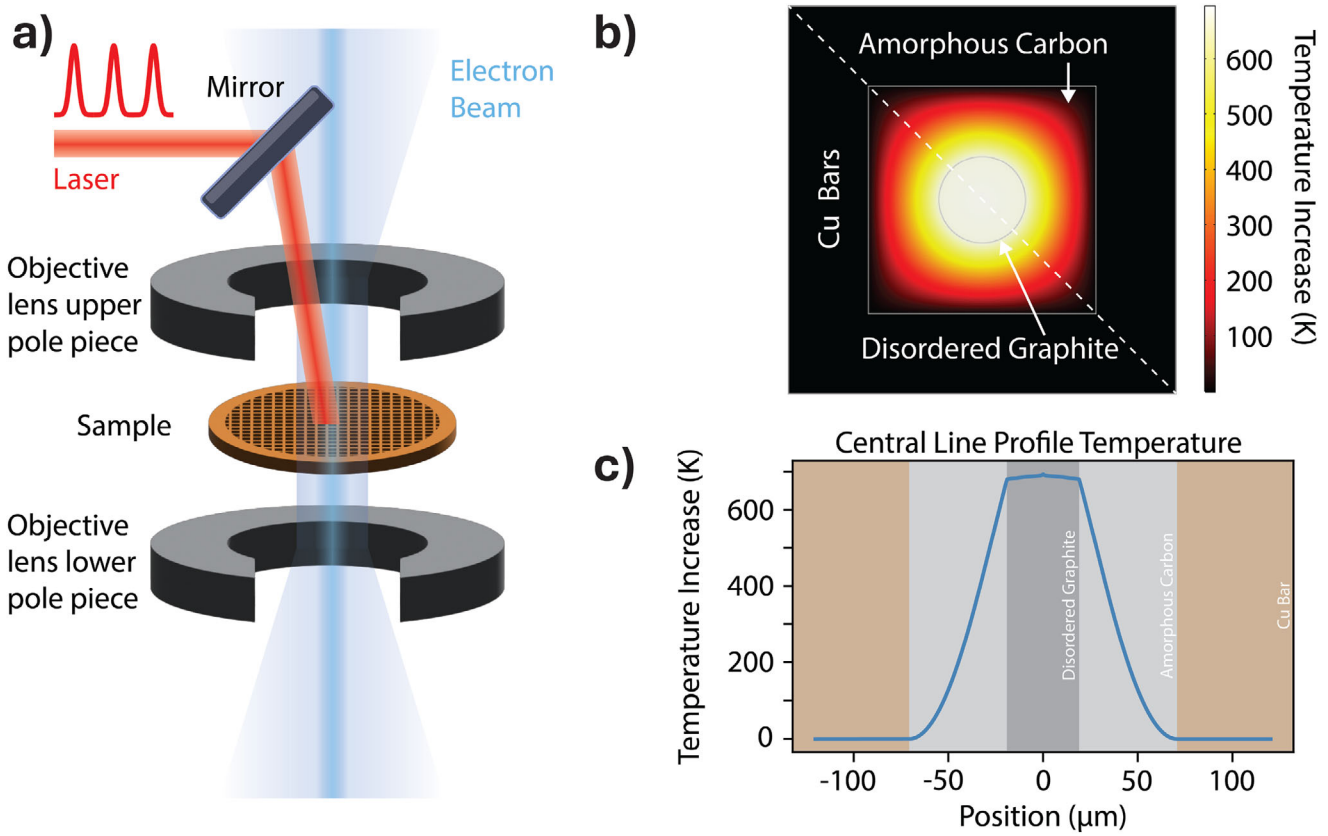



**FIGURE 1** | (a) Modified Transmission Electron Microscope with a light in-coupling unit and a mirror placed at the upper pole piece of the objective lens allowing real-time observation of in situ heating. (b) COMSOL heat simulation at maximum temperature exhibiting the temperature gradient of a single grid square. (c) Temperature profile of the dashed line in (b). A small bump in the center can be seen due to the NR. The contribution to the temperature increase due to the NR alone is shown in Figure S2.

carbon contamination on the nanoparticle surface, which enabled tomography, EDX, and 4D-STEM to be performed sequentially on the same particle. On uncoated nanorods, beam-induced carbon contamination largely originates from the citrate surface ligands, which the electron beam cross-links into an amorphous carbon layer. During $TiO_2$ synthesis, these ligands are largely displaced, and the resulting oxide presents an organic-free outer surface, suppressing this contamination pathway. The particles were drop-casted onto standard Quantifoil R 1.2/20 200-mesh copper TEM grids with a 12 nm carbon support film. Experiments were performed in a modified JEOL NeoARM equipped with a cold field emission gun (CFEG) and an IDES light in-coupling unit. A picosecond laser (700 nm wavelength with a 10 nm bandwidth and 26 MHz repetition rate) was focused onto the sample plane by a focusing lens and a mirror in the TEM column as shown schematically in Figure 1a, allowing the light to hit the sample roughly collinear to the electron beam. The laser was focused to a spot size of around 64 μm (defined as the diameter at which the laser intensity decreases to $1/e^2$ of its peak value), substantially larger than any individual nanoparticle (Figure S1). Under these conditions, the carbon film, which was present across the entire grid window, was the dominant photothermal absorber. While the gold nanorods are themselves efficient photothermal heaters, their nanoscale volume means that their contribution to the overall thermal budget of the window was small compared to the extended carbon film and large laser spot size. COMSOL heat-transfer simulations confirmed that an individual AuNR produced a maximum local temperature increase of only about 25 K under the experimental illumination conditions (Figure S2). The particles were furthermore separated by several μm, indicating that collective heating effects do not significantly influence the overall temperature profile. At the employed repetition rate of 26 MHz, the inter-pulse interval is only 38.5 ns. Because the 12 nm carbon film is thermally thin, it cannot dissipate the deposited heat between pulses and instead reaches a quasi-steady-state elevated temperature, effectively behaving as a continuous-wave heat source despite the pulsed excitation (Figure S3a). COMSOL simulations indicated that at the laser powers used, the carbon film reached temperature increases of approximately 650 K at the center of the illuminated window, decaying to 500 K within 25 μm (Figure 1b,c). The quoted temperature increase of 650 K corresponds to a specific reference at 55% of the laser power, equivalent to an experimental fluence of 7.2 $\mu J/cm^2$ (Figure S1) and serves to indicate the order of magnitude of heating reached in these experiments. The actual temperature varies between individual experiments as the laser fluence is adjusted stepwise throughout each acquisition, as shown in Figure S3b. At these high temperatures, we observed that the amorphous carbon actually partially turned into disordered graphite. Evidence of this transition is shown in Figure S4, where the diffraction rings become sharper under laser illumination. Because



16136829, 0, Downloaded from https://onlinelibrary.wiley.com/doi/10.1002/smll.75977 by Centrum Voor Wiskunde En Info (Cwi), Wiley Online Library on [10/11/2026]. See the Terms and Conditions (https://onlinelibrary.wiley.com/terms-and-conditions) on Wiley Online Library for rules of use; OA articles are governed by the applicable Creative Commons License

graphitization increases the thermal conductivity of the support film, this change was incorporated into the heat-transfer simulations shown in Figure 1b.

It is well established from early in situ heating experiments, conducted on carbon-supported TEM grids before MEMS heating holders became standard, that copper-containing species can form and migrate on carbon films at elevated temperatures. For example, Jernigan et al. and Zhang et al. reported copper migration and agglomeration on carbon supports at 600–700°C [24, 25]. We hypothesize that under laser-induced heating, atomic and sub-nanometer copper species mobilized from the grid can diffuse through the porous $TiO_2$ shell and incorporate directly into the gold lattice. The near-uniform heating across the window (Figure 1b) means that copper-containing species can potentially become thermally activated across a large area simultaneously, not only directly under the nanoparticle. To confirm that our laser conditions are sufficient to mobilize copper from the Quantifoil substrate, we performed control experiments on empty grids in the absence of nanoparticles (Figure S5). Using the identical illumination geometry shown in Figure 1, sparse dark dots appeared on the carbon film after illumination at 3.0 $\mu J/cm^2$ (Figure S5b). Increasing the power to 3.8 $\mu J/cm^2$ caused these dots to grow and agglomerate into larger clusters (Figure S5c,d), with *d*-spacings consistent with $Cu_2O$ rather than metallic Cu as shown in Figure S6. To assess whether the electron beam contributes to oxygen removal from these clusters, a control experiment was performed in which $Cu_2O$ nanoparticles formed by laser irradiation were exposed to a highly converged electron beam for an extended period. No measurable change in lattice spacing was observed before and after beam exposure, indicating that electron-beam-induced reduction of $Cu_2O$ is negligible under our experimental conditions. At the highest laser fluence (18.5 $\mu J/cm^2$) the clusters disappeared from the center of the window and appeared near the cooler grid bar edges (Figure S5e), consistent with the temperature gradient over the grid window (Figure 1b,c). In this case, the center region had reached the sublimation temperature of the copper clusters and the colder outer regions had reached temperatures high enough to form clusters. This demonstrates that the spatial extent of available copper is self-limiting as a result of the temperature gradient across the window.

With this physical picture established, we turn to the behavior of AuNR@$TiO_2$ deposited on the same carbon TEM grids under laser illumination. In this experiment, the laser fluence was increased stepwise throughout each acquisition, allowing morphological changes of individual particles to be followed at different fluences. Each fluence step was maintained until morphological changes ceased, indicating that the particle had reached a stable configuration at that excitation level before the fluence was further increased. It should be noted that the threshold fluence for transformation varied slightly between individual particles due to experimental variations in laser alignment, spot size, nanorod position relative to the laser spot and proximity to the grid bars, which affect local heat dissipation. The observed transformations were therefore governed by the local temperature reached by each particle rather than by a unique fluence or irradiation time value. Representative results are shown in Figure 2a, with the applied laser fluence profile, together with the corresponding percentage of maximum power output for the laser, plotted in Figure 2b. Initially, the laser was applied at a fluence of 4.5 $\mu J/cm^2$ for 40 s, switched off, and then turned back on at the same fluence for another 370 s. The fluence was subsequently increased to 4.8 $\mu J/cm^2$ for 187 s and finally to 5.1 $\mu J/cm^2$ for 88 s. A TEM image of the AuNR@$TiO_2$ before laser illumination is shown in Figure 2a.1.

Under laser exposure, the particle underwent a pronounced morphological transformation. The nanoparticle progressively grew, leading to deformation and noticeable expansion of the surrounding $TiO_2$ shell, indicating that material from outside the nanorod entered through the porous shell, which has an estimated porosity of about 60%–70% (Figures S7 and S8) and accumulated inside (Figure 2a.2–a.4, Movie S1). The $TiO_2$ shell itself deformed but remained intact throughout, consistent with its high vaporization temperature (above 2000°C), which makes it robust under the conditions used here. At higher laser fluence (5.1 $\mu J/cm^2$), the particle partially returned toward its original shape (Figure 2a.5), indicating that part of the incorporated material began to sublimate and leave the particle. This expansion-then-contraction sequence was reproducible across multiple grid windows and different nanorods (Figure S9), with only minor adjustments in laser power required between experiments. For comparison at each illumination step, the corresponding TEM image was thresholded and the particle outline extracted and smoothed with a Gaussian filter (Figure S10). The resulting outlines as a function of time are shown in Figure 2c: the nanorod (blue) clearly expanded to a maximum projected area (orange) before shrinking back toward its original dimensions (yellow) at higher fluence. The exact geometry and volume of the protrusions vary from particle to particle and are strongly influenced by the $TiO_2$ shell. We propose that Cu enters the particle through the most porous or thinnest region of the shell, which subsequently also acts as the preferred pathway for outward expansion of the alloyed particle. As a result, protrusions develop predominantly in regions where the geometrical constraint imposed by the shell is weaker. In contrast, often one side of the particle remains in close contact with the $TiO_2$ shell during the transformation, limiting the deformation of the core. Following Cu sublimation, this persistent contact, together with the tendency of gold to minimize its surface energy, promotes a partial recovery toward the initial particle shape.

Two control experiments were performed to verify that the observed morphological changes result from copper incorporation and are not caused by laser-induced modification of the gold nanorods or by electron-beam effects. First, to test if this is indeed copper entering the Au nanorod, we applied directly a fluence that was above the observed sublimation threshold of the copper-containing clusters on the empty grid (Figure S5e). When directly applying a high laser fluence, such as 8.5 $\mu J/cm^2$ as shown in Figure S11, the original particle completely disappeared, indicating that the sublimation temperature of gold was reached. It is also interesting to observe that the shape of the $TiO_2$ shell remained preserved even after complete sublimation of the gold core, and no noticeable nanorod reshaping or increase in the projected area was detected. This suggests that under higher laser power, the surrounding material on the grid sublimates before it can diffuse into the AuNR@$TiO_2$, and that it is likely indeed copper that causes the nanoparticle changes. Second, the influence of the electron beam was tested by repeating the same



16136829, 0, Downloaded from https://onlinelibrary.wiley.com/doi/10.1002/smll.75977 by Centrum Voor Wiskunde En Info (Cwi), Wiley Online Library on [10/11/2026]. See the Terms and Conditions (https://onlinelibrary.wiley.com/terms-and-conditions) on Wiley Online Library for rules of use; OA articles are governed by the applicable Creative Commons License

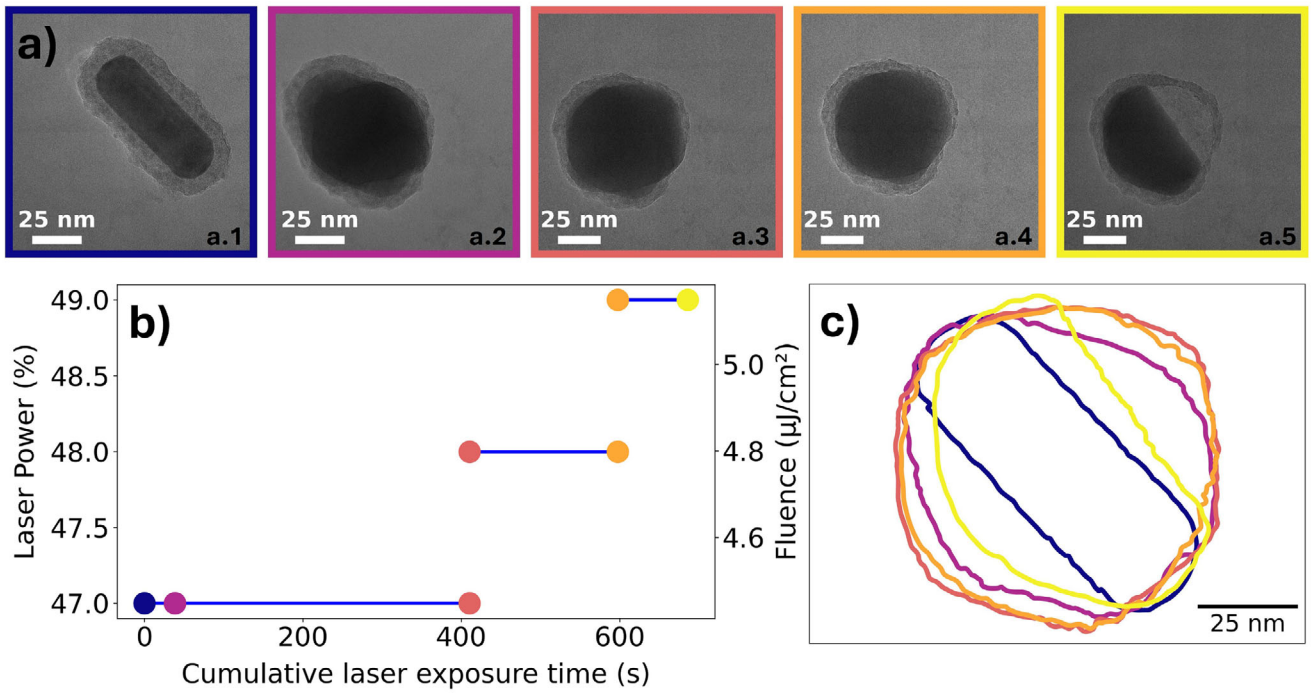



**FIGURE 2** | (a) TEM images of a AuNR@$TiO_2$ under laser exposure: (a.1) before laser exposure, (a.2) after the first laser exposure at 4.5 $\mu J/cm^2$, (a.3) after the second laser exposure at the same fluence, (a.4) after the third laser exposure at 4.8 $\mu J/cm^2$, (a.5) and after the last laser exposure at 5.1 $\mu J/cm^2$. (b) Applied laser power and corresponding calculated fluence (for a laser spot of 64 μm at 26 MHz) as a function of time. The horizontal segments indicate the time intervals during which each laser power was applied. (c) Extracted outline smoothed with a Gaussian filter of the Au nanorod at successive times under laser illumination as in (a).

experiments with the beam switched off during laser irradiation, acquiring images only before and after exposure. As shown in Figure S12, the particle underwent the same transformation as in experiments performed with the beam on, confirming that laser illumination alone is sufficient to drive copper incorporation and alloying. While the absolute kinetics of incorporation may be influenced by the beam, the general findings are independent of beam-induced effects and represent intrinsic behavior of the laser-driven system.

## 2.2 | Volume Evolution and Spatial Distribution

The TEM observations in Section 2.1 suggested that material entered the AuNR@$TiO_2$ under laser illumination, deforming the gold core and expanding the $TiO_2$ shell. If this material was indeed copper incorporating into the gold nanorod, as hypothesized, a direct consequence should be a measurable increase in particle volume. To test this, we performed electron tomography on the same particle shown in Figure 2, acquiring tilt series before illumination and after the first (a.2) and last (a.5) stages of laser exposure. Each tomography series consisted of high-angle annular dark-field scanning transmission electron microscopy (HAADF-STEM) 2D projections acquired from −65° to +65° in steps of 3°. Representative HAADF-STEM images at 0° and ±65° are shown in Figure 3a before (blue a.1), after illumination over 40 s at a fluence of 4.5 $\mu J/cm^2$ (purple a.2) and after the final exposure at 5.1 $\mu J/cm^2$ over 88 s (yellow a.3). After the first exposure, the material visibly spread onto the TEM substrate, resulting in a noticeably flatter interface between the nanorod and the grid at high tilt angles (purple arrows, in Figure 3a.2). Importantly, the $TiO_2$ shell also clearly deformed outward, indicating that the newly incorporated material was growing inside the shell rather than merely depositing on its surface. At higher fluence (Figure 3a.3), the additional material largely disappeared, and the nanorod partially recovered its original shape, consistent with the TEM results in Section 2.1. The same particle imaged with the bright-field detector (a.4) makes the shell deformation particularly clear, as the lower Z contrast of $TiO_2$ is better captured under these detector settings. The tilt series were aligned by cross-correlation and reconstructed using an expectation-maximization algorithm. After segmentation with the Otsu threshold, the particle volume was calculated at each stage. The results are shown in Figure 3b: the volume increased approximately fourfold after the first illumination stage, then decreased to roughly twice the original volume after higher-fluence exposure. This confirms that substantial new material entered the nanorod during laser illumination, and was partially removed at higher fluences, consistent with suspected sublimation of the incorporated copper, which has a lower sublimation point than gold at the operating pressure of the TEM. An independent tomography dataset acquired on a different AuNR@$TiO_2$ particle showed a similar trend, with the particle volume decreasing after continued laser exposure to a value close to the estimated initial volume (Figure S13), further supporting partial recovery of the original morphology following Cu sublimation.

To gain more time-resolved insight into how material is incorporated during illumination, we turn to the HAADF-STEM image series in Figure 3c, acquired on a different particle under laser illumination at stepwise increasing fluence. In HAADF-



16136829, 0, Downloaded from https://onlinelibrary.wiley.com/doi/10.1002/smll.75977 by Centrum Voor Wiskunde En Info (Cwi), Wiley Online Library on [10/11/2026]. See the Terms and Conditions (https://onlinelibrary.wiley.com/terms-and-conditions) on Wiley Online Library for rules of use; OA articles are governed by the applicable Creative Commons License

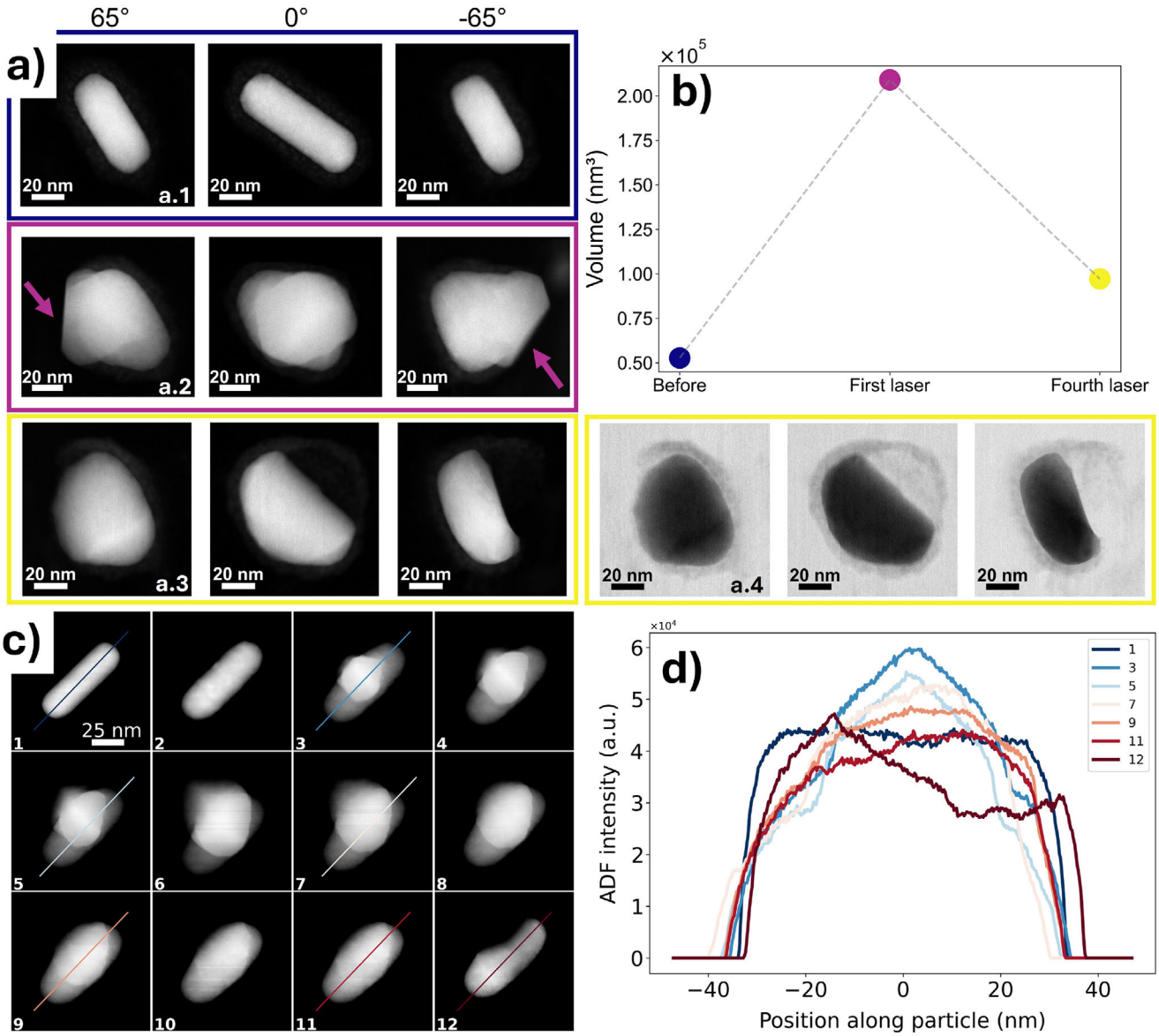



**FIGURE 3** | (a) HAADF-STEM images taken tilting the holder at 0°, +65°, −65° (a.1) before, (a.2) after 700 nm and 26 MHz laser illumination at 4.5 $\mu J/cm^2$ for 40 s and (a.3) after illumination at 5.1 $\mu J/cm^2$ for 88 s. In (a.4) are the same images as in (a.3) but acquired with the bright field detector. (b) Volume of the three 3D reconstructions after binarization. (c) STEM images of another particle (1) before, (2–6) under 700 nm and 26 MHz laser illumination at 5.8 $\mu J/cm^2$ and (7–12) at 7.0 $\mu J/cm^2$. (d) Line profile of the intensity extracted along the same color-coded line in (c).

STEM, image contrast scales monotonically with both specimen thickness and atomic number Z: a higher signal indicates therefore either more material (a thicker nanoparticle) or heavier atoms. Under laser illumination, a region of increased contrast appeared at the center of the nanorod and grew progressively until it extended beyond the original $TiO_2$ shell boundaries (Figures 3c.3–c.7). This high-contrast region most likely reflects growth in the third dimension: copper entering through a weak point in the $TiO_2$ shell and accumulating preferentially along the path of least resistance caused the particle to thicken out of plane rather than expanding uniformly in the image plane. This is directly visible in the line profiles extracted along the center of the nanorod shown in Figure 3d: a sharp, localized increase in intensity appeared in the middle of the rod corresponding to the protrusion (blue line 3), while the intensity along the rest of the rod evolves differently, pointing to distinct physical origins of the contrast changes in the two regions. This interpretation is further supported by observations of other particles where the protrusion was clearly anisotropic and visible predominantly in one direction in 2D projection (Figure S9). Critically, the in-plane portion of the original gold core, the region of the nanorod away from the protrusion, simultaneously showed a reduction in contrast compared to before illumination. These two contrast changes occurred in different spatial regions of the particle: the protrusion grew where copper entered through the shell, while the remaining gold core dimmed uniformly, pointing to a compositional change, specifically, dilution of the Au lattice by the lighter Cu atoms through alloying. The line profiles in Figure 3d confirm that this contrast reduction is spatially uniform across the in-plane rod from early on in the illumination sequence, indicating that copper incorporated homogeneously throughout the nanorod volume rather than accumulating as a



16136829, 0, Downloaded from https://onlinelibrary.wiley.com/doi/10.1002/smll.75977 by Centrum Voor Wiskunde En Info (Cwi), Wiley Online Library on [10/11/2026]. See the Terms and Conditions (https://onlinelibrary.wiley.com/terms-and-conditions) on Wiley Online Library for rules of use; OA articles are governed by the applicable Creative Commons License

segregated surface layer. At higher laser power (Figure 3c.8–c.12), both effects reversed: the sharp intensity peak in the line profile corresponding to the out-of-plane protrusion disappeared and the in-plane contrast of the gold core recovered toward its original level, consistent with sublimation of the incorporated copper, which has a substantially higher vapor pressure than gold at the temperatures reached [25]. Based on the Clausius–Clapeyron equation, at 1100 K the vapor pressure is approximately $1.89 \times 10^{-4}$ Pa for pure Cu and $7.06 \times 10^{-6}$ Pa for pure Au.

Together, the tomography and STEM series established that laser illumination drives a substantial and reversible volumetric change in the AuNR@$TiO_2$. Furthermore, the incorporated material is distributed homogeneously through the particle from early stages. Based on the control experiments in Section 2.1, we attribute this material to copper migrating from the substrate. To directly confirm this assignment, EDX maps were acquired on a different particle before and after successive illumination stages at increasing power (Figure S14a). The total gold signal remained constant throughout despite the particle growing in size, while the copper signal increased substantially during the first two exposures and subsequently decreased at higher fluence. Since EDX signal scales with the amount of material present, the constant gold signal rules out gold redistribution as the source of the volume increase, and the rising copper signal directly confirms that the incorporated material is copper. Quantitative fitting of the characteristic X-ray lines (AuL $_\alpha$, AuM $_\alpha$, CuK $_\alpha$, CuL $_\alpha$) confirms this trend unambiguously (Figure S14d). Control experiments assessing the contribution of the copper signal from the TEM grid bars and from the microscope column due to secondary scattering are shown in Figure S15.

## 2.3 | Composition Control and Alloy Homogeneity

Having established that copper incorporates into the AuNR@$TiO_2$ under laser illumination, the key remaining question is whether it forms a spatially homogeneous alloy with gold or remains segregated, for instance accumulating preferentially in the region of the protrusion. To address this at the spatial resolution accessible by EDX, summed X-ray counts were extracted from several distinct regions across a single nanoparticle that developed a large protrusion after laser-induced alloying (Figure S16a). As shown in Figure S16b,c, both the gold and copper signals remained uniform across all sampled regions, indicating that copper was distributed evenly throughout the particle at this length scale rather than concentrated in any particular zone. This points toward homogeneous alloying rather than core–shell segregation or surface decoration. However, EDX spatial resolution is insufficient to assess atomic-scale mixing, and the question of whether gold and copper are truly intermixed at the lattice level, rather than forming nanoscale phase-separated domains, cannot be answered by EDX alone. We therefore turn to electron diffraction, which is sensitive to the lattice parameter of the alloy and can quantify the copper fraction through Vegard's law [26].

Both gold and copper crystallize in the FCC structure with well-separated lattice parameters (Au at $a$ = 407.82 pm and Cu at $a$ = 361.49 pm, corresponding to (111) d-spacings of 0.235 nm and 0.208 nm, respectively). As a result, copper incorporation into the gold lattice produces a measurable contraction of the lattice parameter that can be tracked in real time through the positions of diffraction spots. To measure diffraction spacings, consecutive electron diffraction patterns were acquired using the TimePix3 pixelated detector on a single AuNR@$TiO_2$ while the laser was on, with a stepwise laser fluence increase from 5.5 $\mu J/cm^2$ to 13.5 $\mu J/cm^2$. It is worthy to mention that these are slightly higher fluences compared to the experiments in Figures 2 and 3. These higher fluences were required to achieve the same particle modifications as observed before, likely due to a slight misalignment in the laser on the day of the experiments. Between each fluence increment, a TEM image of the particle was acquired to monitor morphological changes; representative images at selected illumination stages are shown in Figure 4a, confirming the same expansion-then-contraction reshaping sequence described in Section 2.1. The laser power profile and corresponding fluence are shown in Figure 4b. A representative diffraction pattern is shown in Figure 4c: it contains sharp diffraction spots arising from the crystalline nanorod, superimposed on two broad amorphous rings from the carbon substrate, which were observed to sharpen progressively under laser heating as amorphous carbon partially graphitized.

The positions of individual diffraction spots were tracked across all illumination steps by fitting a 2D Gaussian to each spot and computing its radial distance from the center of mass (COM) of the diffraction pattern (Figure 4c, colored overlays). All tracked reflections show the same trend: a progressive outward radial shift up to the fourth illumination step, followed by a gradual return toward the initial positions at higher fluence. Since an outward shift corresponds to a smaller d-spacing by Bragg's law, this directly reports lattice contraction consistent with copper incorporation. The d-spacing for the two reflections closest to the COM is plotted as a function of illumination time in Figure 4d: it decreases from 0.235 nm, consistent with pure gold, to a minimum of approximately 0.215 nm, before recovering toward the initial value at higher fluence. Applying Vegard's law to the minimum d-spacing of 0.215 nm yields a copper fraction of approximately 75%. It should be noted that the same trend is followed by all the diffraction reflections tracked in the pattern as shown in Figure S17.

Since these diffraction patterns were recorded while the laser was on, thermal expansion of the lattice partially counteracted the compositional contraction, causing the copper fraction to be underestimated. To decouple these effects, additional diffraction patterns were acquired with the laser switched off on the same particle after some of the illumination steps, allowing the substrate to return to room temperature between measurements. The laser-off series (Figure S18) shows the same trend: initial d-spacing decrease followed by recovery. It should be noted that laser-off diffraction data were only recorded after specific laser exposure steps. When comparing the laser-on and laser-off measurements after the second laser exposure step, the estimated copper fraction increased from approximately 70% under laser illumination to approximately 80% once the laser was switched off, highlighting the significant influence of thermal expansion during irradiation. Since the laser-on data reached a minimum d-spacing at the end of the third laser exposure step, where no corresponding laser-off diffraction pattern was acquired, it is reasonable to expect an even higher copper content when thermal



16136829, 0, Downloaded from https://onlinelibrary.wiley.com/doi/10.1002/smll.75977 by Centrum Voor Wiskunde En Info (Cwi), Wiley Online Library on [10/11/2026]. See the Terms and Conditions (https://onlinelibrary.wiley.com/terms-and-conditions) on Wiley Online Library for rules of use; OA articles are governed by the applicable Creative Commons License

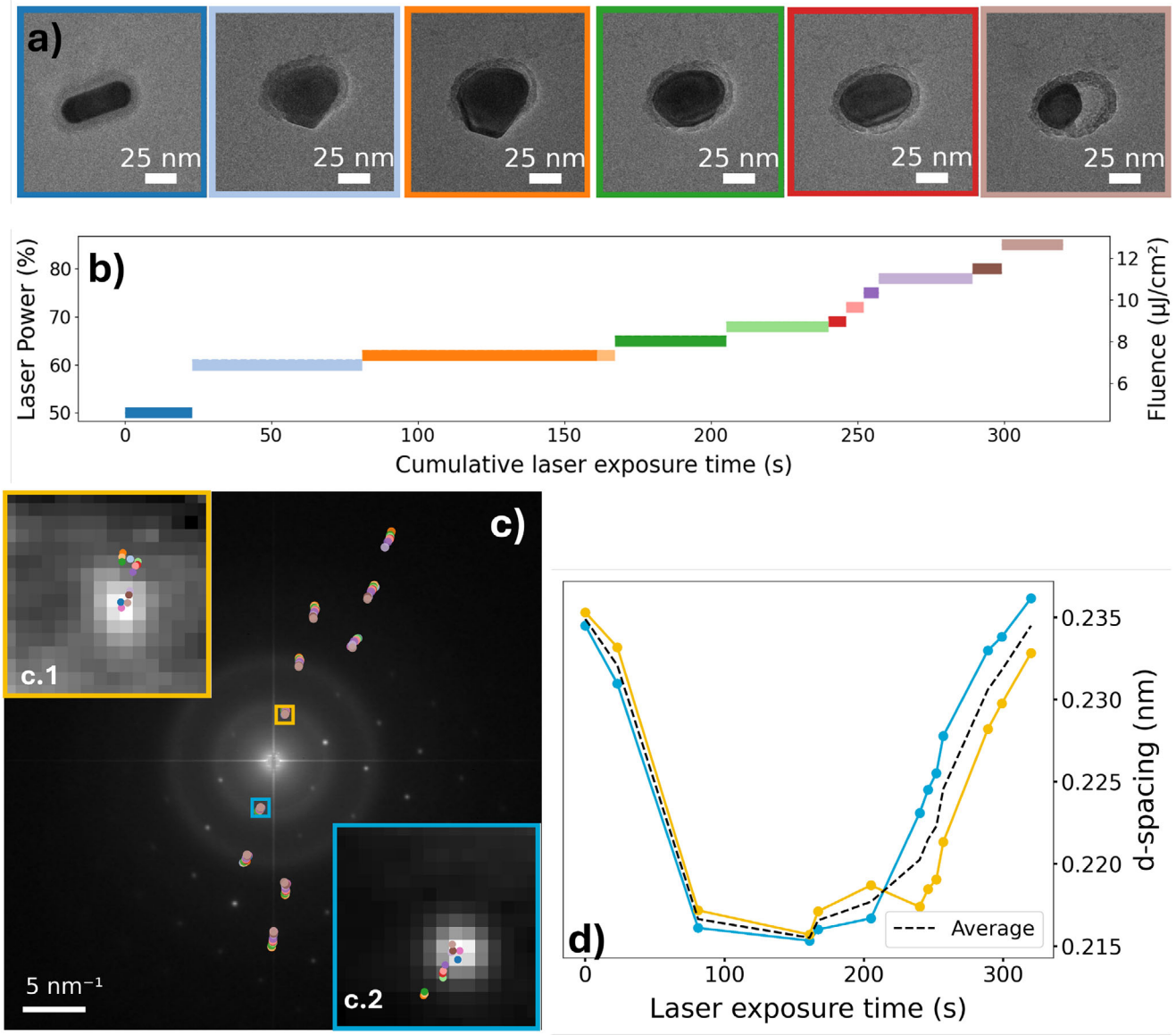



**FIGURE 4** | Diffraction under laser illumination (a) TEM images of the NR at different stages of laser illumination (b) Exposure time for each laser step. On the y axis the respective laser power and fluence are shown, while the x-axis represents the cumulative illumination time for each laser exposure step. (c) Positions of diffraction spots tracked from the last diffraction pattern acquired in each laser exposure step shown in (b), overlaid on the diffraction spectra acquired before laser exposure. The colors of the tracked diffraction spots correspond to the laser exposure step colors shown in (b), with bright pink indicating the dataset acquired prior to any laser illumination. In c.1 and c.2 a zoom in on the two diffraction spots closest to the COM is shown, highlighting the change in position of the diffraction dots as a function of laser exposure. (d) d-spacing as a function of laser illumination time for the two diffraction dots in (c) is shown. The dotted line represents the average of the two diffraction spacings to account for sub-pixel errors.

contributions are removed. Based on the observed trend, the copper fraction at this stage is therefore estimated to approach 85% under laser-off conditions. This fraction is consistent in order of magnitude with the fourfold volume increase measured by tomography in Section 2.2. Given similar atomic volumes of Au and Cu, a fourfold volume increase implies a composition of approximately 25% gold and 75% copper, in good agreement with the diffraction result. We note that the absolute copper fraction will vary between particles depending on the amount of copper locally available from the surrounding substrate, and the comparison between tomography and diffraction involves different particles measured under slightly different conditions. Nevertheless, the quantitative consistency across these independent measurements strengthens our conclusion that a high copper fraction, on the order of 75%–85%, can be achieved under laser illumination. Furthermore, from the difference in d-spacing measured under laser-on and laser-off conditions, we were able to experimentally estimate the temperature reached during laser irradiation. Thermal expansion leads to a lattice change according to $\Delta d/d = \alpha\,\Delta T$, where $\alpha$ is the linear thermal expansion coefficient. For the calculation, $\alpha$ was varied between $1.4 \times 10^{-5}\,\mathrm{K}^{-1}$ (pure Au) and $1.6 \times 10^{-5}\,\mathrm{K}^{-1}$ (pure Cu) based on the alloy composition estimated from the diffraction data. Using the measured difference in d-spacing between laser-on and laser-off conditions yields an estimated temperature increase of $\Delta T \approx 800\,\mathrm{K}$. This value is in good agreement with the temperatures



16136829, 0, Downloaded from https://onlinelibrary.wiley.com/doi/10.1002/smll.75977 by Centrum Voor Wiskunde En Info (Cwi), Wiley Online Library on [10/11/2026]. See the Terms and Conditions (https://onlinelibrary.wiley.com/terms-and-conditions) on Wiley Online Library for rules of use; OA articles are governed by the applicable Creative Commons License

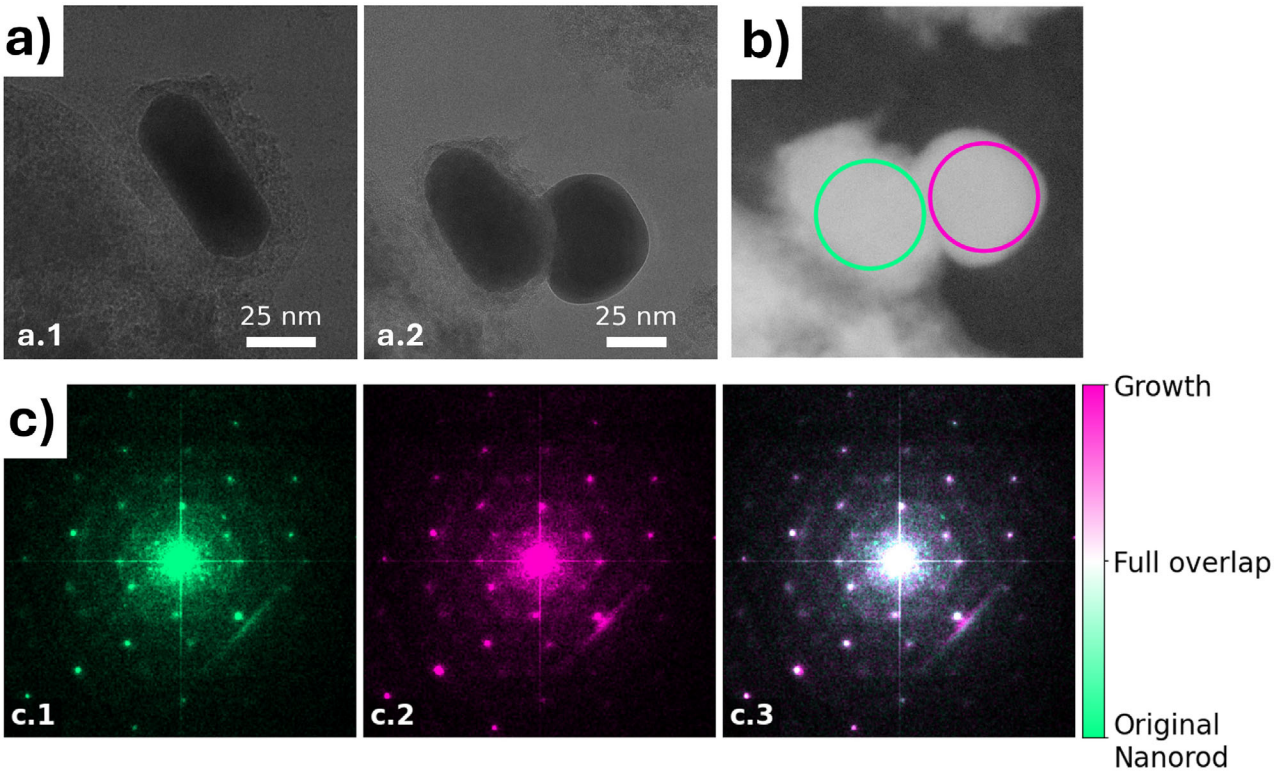



**FIGURE 5** | (a) HR−TEM image of a AuNR@$TiO_2$ before laser illumination (a.1) and after irradiation of the maximum laser power of 5.5 $\mu J/cm^2$ (a.2) and (b) STEM image of the same AuNR@$TiO_2$ in a.2 (c) Diffraction patterns, after logarithmic normalization and percentile-based contrast enhancement, obtained from the regions indicated by the circles in (b). (c.1) Pattern from the area inside the green circle. (c.2) Pattern from the area inside the pink circle. In (c.3) the two diffraction patterns are overlayed to highlight differences, with green indicating signal unique to (c.1), magenta unique to (c.2), and white indicating full overlap between the two patterns.

predicted by the heat simulations shown in Figure S3. Finally, Figure S18 shows that the lattice spacing measured after prolonged sublimation remains slightly smaller than that of pure Au, indicating that the particle does not return completely to the pure-gold state and that a residual amount of Cu remains dissolved in the alloy.

From the EDX and diffraction analyses, we estimate above 80% of copper being incorporated into the gold nanorod under our experimental conditions. To further probe local compositional homogeneity and crystal orientation homogeneity, we performed 4D-STEM experiments in quasi-parallel nano-beam diffraction mode, which provides a diffraction pattern at each probe position and allows comparison of local lattice parameters across the particle. TEM images of the chosen AuNR@$TiO_2$ before (Figure 5a.1) and after (Figure 5a.2) laser illumination show that a large protrusion developed during illumination, extending well beyond the original $TiO_2$ shell boundary. This outward growth indicates that gold atoms redistributed beyond their original confinement to participate in forming the alloy, a finding consistent with the strongly negative mixing enthalpy of AuCu at the nanoscale, which makes Au–Cu bond formation energetically favorable over maintaining a pure gold core adjacent to a copper-rich exterior [8]. The virtual dark-field image reconstructed from the 4D-STEM dataset is shown in Figure 5b, confirming the spatial extent of the crystalline material after illumination.

Diffraction patterns extracted from two distinct regions, the original nanorod interior (green, Figure 5c.1) and the newly grown material outside the original shell (magenta, Figure 5c.2), are compared in Figure 5c.3, where they are additively overlaid. In this representation, green indicates signal unique to the original rod position, magenta indicates signal unique to the grown region, and white indicates full overlap. The two patterns overlap almost completely, with the only deviation occurring at small radial distances, where $TiO_2$ diffraction was present exclusively in the original rod region, corresponding to the shell. The near-perfect overlap of the diffraction patterns from both regions demonstrates that the original nanorod and the newly grown material share the same contracted lattice parameter: they are crystallographically indistinguishable and form a single homogeneous AuCu solid solution. To quantify this, diffraction spot positions in both patterns were determined by 2D Gaussian fitting and the radial displacement $\Delta r$ between corresponding reflections in the two regions was calculated (Figure S19). All reflections show $\Delta r$ values close to zero, with no systematic trend, confirming that there is no measurable lattice parameter difference between the original rod location and the grown material and that copper is homogeneously distributed throughout the particle at the length scale accessible by this measurement.

Together, the EDX, diffraction, and 4D-STEM analyses established that laser illumination drives the formation of a spatially homogeneous AuCu solid solution throughout the nanorod and



16136829, 0, Downloaded from https://onlinelibrary.wiley.com/doi/10.1002/smll.75977 by Centrum Voor Wiskunde En Info (Cwi), Wiley Online Library on [10/11/2026]. See the Terms and Conditions (https://onlinelibrary.wiley.com/terms-and-conditions) on Wiley Online Library for rules of use; OA articles are governed by the applicable Creative Commons License

any outgrown protrusion, with an achievable copper fraction above 80%. With this complete picture of the alloying process assembled, we now turn to a discussion of the incorporation and removal mechanism and its implications for compositional control. The $Cu_2O$ clusters observed on the carbon support under laser illumination (Figures S5 and S6) provide a source of copper. While the precise chemical pathway by which Cu migrates from the substrate and incorporates into the Au nanorod cannot be determined from the present data, previous studies have shown that copper oxides can be reduced under vacuum annealing conditions, with metallic Cu appearing above 670 K [27]. At the temperatures estimated during laser illumination (approximately 1000 K) and the negligible oxygen partial pressure in the TEM column, these oxide species are therefore readily reduced to metallic copper under our conditions. Furthermore, the Au–Cu system has a strong thermodynamic tendency toward alloy formation due to its negative enthalpy of mixing, making the alloyed state energetically more favorable than phase segregation [28].

The incorporation and removal of copper are intrinsically asymmetric processes, as shown in Figure 3c,d and Figure 4d, where a comparatively rapid shift toward a Cu-rich alloy during the early heating steps is followed by a more gradual recovery toward pure Au at higher fluences. However, since Figure 4d only represents the endpoint diffraction pattern acquired at the conclusion of each fluence step, it does not capture how composition evolves continuously within a given exposure. To resolve this, we show three different diffraction series (Figure S20), in which patterns were acquired during laser illumination, providing a full temporal trajectory of composition rather than just end-points. These snapshots demonstrate that incorporation occurs on a much faster timescale compared to the removal phase, visible in a clear and measurable asymmetry in the kinetics of the two processes.

The incorporation timescale reflects a coupled sequence of processes: the thermal activation and melting of neighboring copper-containing clusters under laser heating, transport of copper species to the AuNR surface, and interdiffusion and alloy formation throughout the nanorod volume. That incorporation is mainly completed within a single illumination step of ten seconds (Figure S20b.1) is consistent with what is expected from diffusion theory. At the temperatures reached (about 1000 K), literature values of Cu in Au diffusion coefficients (D) are on the order of $10^{-14}$ $m^2/s$, depending on alloy composition [29]. Based on Fick's law of diffusion ($\langle r^2 \rangle = 6Dt$), these values correspond to characteristic diffusion times (t) of approximately 10 ms and 94 ms across the short ($r = 25$ nm) and long ($r = 75$ nm) axes of the nanorod, respectively. Internal diffusion is therefore not rate-limiting, and the observed incorporation timescale is instead likely governed by the supply of copper from the surrounding substrate, making it sensitive to local geometry: particles with more proximal copper sources will incorporate faster independently of any intrinsic diffusion rate.

The slower removal, by contrast, is governed by surface evaporation rather than by diffusion. At the temperatures required for sublimation, internal diffusion remains fast, and copper equilibrates across the particle in tens of milliseconds. Although Cu is preferentially removed, the Au–Cu system has a strong thermodynamic tendency toward alloy formation due to its negative enthalpy of mixing [28]. Combined with the rapid internal diffusion at these temperatures, this favors a homogeneous alloy composition rather than the development of Au-rich and Cu-rich regions. Cu lost from the surface is therefore continuously replenished from the particle interior, helping to maintain a homogeneous alloy composition while preferential Cu sublimation proceeds [29]. The rate-limiting step is therefore assumed to be the evaporative flux from the nanoparticle surface, which can be estimated, within order of magnitude, using the Hertz–Knudsen equation (see Supporting Information for details). As an illustrative example, the calculation is performed for the laser illumination interval corresponding to the light-green region in Figure S20a, whose lattice-spacing evolution is shown in Figure S20b.2. Assuming that the Au content remains constant throughout the experiment, the lattice spacings measured at the end of the preceding dark-green illumination step and at the end of the light-green illumination step are used to determine the amount of Cu lost by evaporation during this interval. Using representative temperatures between 1100 and 1150 K, obtained from the laser-induced lattice expansion as described above, the model predicts evaporation times between 81 and 22 s (Table S3). This range is in reasonable agreement with the experimentally observed timescale of approximately 35 s and highlights the strong sensitivity of the evaporation process to temperature.

Taken together, these observations reveal two complementary and independently tunable handles on alloy composition. Laser fluence sets the thermodynamic window, determining whether the system sits in a regime where incorporation dominates or where evaporative loss becomes significant. Illumination time controls how far the composition evolves within that window. Because evaporation requires substantially higher fluences and longer times than incorporation, the alloy composition is kinetically robust against small perturbations in laser power once formed, and can be driven back toward pure Au only by deliberate escalation of fluence. Switching the laser off at any point kinetically traps the current composition indefinitely, providing a practical and flexible route to targeting a desired Cu fraction at the single-particle level.

## 3 | Conclusion

This work demonstrates that pulsed optical excitation enables dynamic, reversible control over the composition of individual bimetallic nanoparticles, as directly visualized in situ by transmission electron microscopy. Specifically, we show that Au nanorods encapsulated in a $TiO_2$ shell can incorporate copper from the surrounding substrate under laser illumination, forming a homogeneous AuCu solid solution with tunable composition. Through a combination of TEM imaging, electron tomography, EDX, and diffraction analysis, we established that laser-induced heating drove substantial and reversible structural and compositional changes. Copper incorporation led to pronounced volumetric expansion and lattice contraction consistent with alloy formation, reaching Cu fractions above 80%. At higher laser fluences, partial removal of copper via sublimation restored the system toward its initial Au-rich state. Importantly, 4D-STEM and diffraction measurements confirmed that the resulting alloy was spatially homogeneous across the particle, rather than phase-segregated. The maximum Cu fractions achieved are likely not an intrinsic



16136829, 0, Downloaded from https://onlinelibrary.wiley.com/doi/10.1002/smll.75977 by Centrum Voor Wiskunde En Info (Cwi), Wiley Online Library on [10/11/2026]. See the Terms and Conditions (https://onlinelibrary.wiley.com/terms-and-conditions) on Wiley Online Library for rules of use; OA articles are governed by the applicable Creative Commons License

limit of the alloying process, but are instead constrained by the finite availability of copper in the local region of the TEM window, which acts as the material reservoir.

The alloying process was governed by asymmetric kinetics: rapid incorporation of copper at moderate fluence, followed by slower removal at higher fluence. This asymmetry provides two independent control parameters, laser fluence and illumination time, enabling precise tuning of composition. Once the laser is switched off, the alloy state is kinetically trapped at room temperature, allowing intermediate, non-equilibrium compositions to be stabilized on demand. Beyond demonstrating a novel route to achieve high Cu incorporation in Au nanoparticles, this study demonstrates the potential of optical excitation as a tool for actively controlling material composition at the single-particle level. The ability to reversibly drive and freeze alloy states opens new opportunities for tailoring catalytic, plasmonic, and electronic properties in situ. Future work will focus on systematically disentangling the effects of laser fluence, irradiation time, and pulse repetition rate on the local temperature evolution and resulting alloying/dealloying behavior. This will enable the establishment of quantitative transformation thresholds and kinetic models for laser-driven compositional control at the single-particle level. Furthermore, while the present experiments were performed at a high repetition rate, making the laser effectively quasi-continuous-wave (CW), experiments at lower repetition rates could provide further insight into kinetic trapping by allowing the particle to cool between successive pulses. Finally, the same approach can be applied to other material systems, including immiscible alloys, to explore laser-driven pathways toward metastable compositions and nanostructures that are inaccessible under equilibrium conditions.

## 4 | Experimental Section

### 4.1 | Growth of an Amorphous Titania Shell Around Au Core Nanorods

#### 4.1.1 | Chemicals

All starting materials were used without further purification. Titanium chloride(III) ($TiCl_3$) solution 15% in 10% hydrochloric acid for synthesis, and 99.7% sodium bicarbonate were purchased from Sigma–Aldrich. Citrate capped nanorods of $25 \times 75$ nm with a density of $7.93 \times 10^8$ NP/mL were purchased from Nanopartz. Milli-Q grade water (resistivity 18.2 M Ω cm at 25 °C) was used in all experiments.

#### 4.1.2 | Synthesis

The colloidal growth of an amorphous $TiO_2$ shell around citrate capped gold NRs was carried out following a protocol adapted from Wu et al. [30] and Fang et al. [31]. 3 mL of $25 \times 75$ nm citrate capped nanorods stock solution were left sinking over one week. After one week the supernatant was removed and the bottom of the solution was collected and re-dispersed in 200 μL of Milli-Q water. The precursor $Ti^{3+}$ solution was prepared by adding 100 μL of 15% $TiCl_3$ to 4 mL of Milli-Q water under vigorous stirring to ensure complete mixing. The pH of the resulting reddish solution was measured to be 1.4 using a Hanna Piccolo pH meter. Under maximum stirring, 460 μL of 1 M $NaHCO_3$ solution was added dropwise. Adding the bicarbonate solution to the $TiCl_3$ solution slowly was crucial to avoid precipitation of $TiO_2$ in solution. After the first addition of 400 μL, the solution turned transparent, and the pH was measured to be 2.43.

A few seconds were allowed to pass before adding the remaining 60 μL of 1 M $NaHCO_3$ solution. After this addition, the solution immediately turned blue, with a measured pH of 2.9, indicating that $Ti^{3+}$ cations had formed in solution. 500 μL of the citrate capped gold nanorods dispersed in water were immediately added while keeping vigorous stirring. The negative surface charge of the citrate layer [32] attracts the positively charged $TiO_2$ cations resulting in growth of a shell around the NRs. After seven minutes, the solution was placed in Eppendorf tubes and centrifuged at 6000 rpm for 5 min. The supernatant was removed and re-dispersed in Milli-Q water. The cleaning procedure was repeated three times.

### 4.2 | Instrumentation

The experiments reported were performed in an aberration-corrected NeoARM (S)TEM with Cold Field Emission Gun (CFEG, 0.3 eV FWHM energy spread), operated at 200 kV. The BF-TEM images were acquired on a TVIPS XF416 R(ES) bottom mounted camera. STEM images were acquired with an annular bright field (ABF) or an annular dark field (ADF) detector.

#### 4.2.1 | Light In-Coupling Unit

The microscope is equipped with a JEOL–IDES Luminary laser in-coupling unit composed of a fiber-coupled laser, an inlet port, and a compact optical delivery system with a mirror to adjust the position of the laser spot and a collimator to focus the beam onto the sample. Laser alignment was performed using the JEOL–IDES fluorescent (PLAH) holder, which enables direct visualization of the laser spot and alignment with the electron beam. The laser used in this work was an NKT FIU-15 combined with an NKT VARIA tunable filter from 400 to 840 nm. The pulse length varies between 20 and 100 ps depending on wavelength, while the repetition rate can be tuned from 0.15 to 78 MHz.

A typical experiment consisted of acquiring consecutive TEM images under pulsed laser illumination while varying the fluence by adjusting the peak laser power between 40% and 80% of the maximum power. For the measurements reported here, we used a wavelength of 700 nm with 10 nm bandwidth and a repetition rate of 26 MHz, corresponding to 38.5 ns in between pulses. At this wavelength the pulse length is around 22 ps. The laser was focused onto the sample with a spot size of 40 μm FWHM and 64 μm ($1/e^2$), as determined from a 2D Gaussian fit of the laser spot as shown in Figure S1a. The laser power settings (measured power at the fiber output and calculated peak fluence at the sample) are summarized in Table S2.

The power measured at the fiber output before entering the TEM was used to calculate the fluence in $\mu J/cm^2$, assuming a Gaussian beam, values are reported in Figure S1b. The average laser output



16136829, 0, Downloaded from https://onlinelibrary.wiley.com/doi/10.1002/smll.75977 by Centrum Voor Wiskunde En Info (Cwi), Wiley Online Library on [10/11/2026]. See the Terms and Conditions (https://onlinelibrary.wiley.com/terms-and-conditions) on Wiley Online Library for rules of use; OA articles are governed by the applicable Creative Commons License

power was measured with a power meter at discrete percentage of the peak power, between 30% and 100% in steps of 10%. Assuming constant pulse energy at different repetition rates, the average power corresponding to each repetition rate was estimated. Finally, fluence values at intermediate power-percentage settings were obtained by linear interpolation between adjacent measured data points. This interpolation provides an approximation, since the relationship between power percentage and average output power is not strictly linear. Since the power cannot be measured inside the column, the actual fluence at the sample is expected to be slightly lower due to optical losses in the IDES unit. During illumination, images were recorded every few seconds over hundreds of seconds; at 26 MHz, this corresponds to $2.6 \times 10^7$ pulses per second.

The exact fluence for the same laser settings varied slightly from experiment to experiment, however, we note that even with these slight variations, the same qualitative trends are seen every time. Reasons for these small variations are the following. First, changes in laser alignment on the order of several μm may occur. As seen in Figure S1a, a laser spot increasing from 64 to 100 μm leads to a dramatic change in fluence. Furthermore, the exact position within the window of the NR under examination plays an important role. Although all studied AuNRs@$TiO_2$ were located near the center of the window, the exact distance from the copper bar strongly affects heat dissipation. Since copper acts as a heat sink, the closer the particle is to the bar the faster the Quantifoil substrate cools down, and the less the sample heats up as shown in Figure 1b,c. Therefore, a unique quantification of reshaping as a function of fluence and temperature is not straightforward. Nevertheless, all experiments showed consistent qualitative trends, with only minor variations in the exact peak power required to induce reshaping.

#### 4.2.2 | Diffraction and 4D-STEM

A transmission electron microscope (TEM) equipped with scan coils can perform 4D-STEM when paired with a direct or pixelated detector. In this technique, a 2D diffraction pattern is acquired at each probe position, resulting in a four-dimensional dataset (two spatial dimensions × two reciprocal-space dimensions), hence the name *4D-STEM* [33]. Experiments were recorded using an ASI Timepix3 detector. This detector is a hybrid pixel detector: an event-driven direct electron detector with an event detection resolution of 1.56 ns. It is composed of four chips with 256 × 256 in each quadrant operating in an event-based mode.

A parallel beam is used in all 4D-STEM diffraction data presented in this paper. This allows distinct diffraction spots as opposed to broadened disks when using a converged beam. The diffraction data acquired on the TimePix detector were treated in the following manner. First, the center of mass (COM) of each diffraction pattern was calculated and then used to align every image to each other to account for any shift of the direct beam in between measurements. The main diffraction peaks of each image were then detected. A Gaussian was fitted in a window of 7 ×7 pixels around the pixel with the highest intensity to detect the center of each diffraction spot. The corresponding reflections from different data sets were then clustered together across every illumination step. Finally, the distance from the COM to the fitted peaks was calculated.

#### 4.2.3 | Energy Dispersive X-Ray Spectroscopy (EDX)

Energy Dispersive X-ray (EDX) data were acquired on the JEOL DrySD100GV EDX detector (100 $mm^2$, windowless, 133 eV@Mn $K_\alpha$ resolution). To analyze the EDX data, the standard procedure described in HyperSpy [34] was followed. First, a model was created using the function create_model(). This automatically generates one Gaussian for each X-ray line, along with a polynomial to represent the background. The widths and energies of the lines were fixed, while the heights of the sub-X-ray lines were linked to their corresponding main α-lines. The model can then be fitted, and the background fitting can be further refined using the fit_background() function which selects only energy ranges that do not contain X-ray lines. The widths of the X-ray lines were determined from the energy resolution (FWHM at Mn $K_\alpha$) specified in the metadata. This parameter can be calibrated by fitting to a reference spectrum.

#### 4.2.4 | Electron Tomography

For the electron tomography experiments, images were acquired with alpha tilts between ±65° with 3° steps. The wide gap pole piece configuration allows higher ranges of tilting for tomography. The 2D projections serve as input for reconstruction algorithms to retrieve the 3D shape. The acquired 2D projection images were first aligned using a cross-correlation-based algorithm. After alignment, the background was removed by subtracting the median of the intensity histogram, followed by detector shadowing and cupping artifact compensation. The cupping correction utilizes an algorithm based on Van Den Broek et al. [35]. The corrected projections then served as input for the reconstruction algorithms. In these experiments the Expectation Maximization (EM) algorithm was employed. EM reconstructions were based on the implementation included in the Astra Toolbox [36] and we used 15 iterations to avoid noise overfitting [37]. The obtained reconstructions were smoothed using a Gaussian filter and segmented using the Otsu method.

### 4.3 | Heat Simulations

Heat simulations were conducted with COMSOL v5.5. The geometry simulated is displayed in Figure 1b. Briefly, we simulated a 100 μm wide carbon thin film surrounded by copper grid bars (35 μm). The thickness of the carbon film was 12 nm, and a gold nanorod was placed in the center of the TEM window. The amorphous carbon was experimentally observed to turn into disordered graphite under laser exposure. Therefore, we defined the center of the window as disordered graphite to match these experimental observations. The material parameters used as input for the simulations are reported in Table S1.

The temperature increase was computed with the module for the heat transfer in solids. We defined two heat sources, one



16136829, 0, Downloaded from https://onlinelibrary.wiley.com/doi/10.1002/smll.75977 by Centrum Voor Wiskunde En Info (Cwi), Wiley Online Library on [10/11/2026]. See the Terms and Conditions (https://onlinelibrary.wiley.com/terms-and-conditions) on Wiley Online Library for rules of use; OA articles are governed by the applicable Creative Commons License

for the nanoparticle and one for the carbon substrate. For the nanoparticle, it was defined as the product of its absorption cross section with the laser fluence. For the carbon, we calculated the absorbed power with the Beer–Lambert law assuming an absorption coefficient of 2919 $cm^{-1}$. The heat source for the thin film was a 2D gaussian. Finally, the temperature was computed with a steady-state simulation.

The solution of the steady-state study was further used as initial temperature condition for the time-dependent study displayed in Figure S3a. We observed that it takes about 2 ms for the system to cool down to room temperature. This shows that the cooling time is much longer than the time in between the pulses (38.5 ns).


### Acknowledgments

This work was part of the research program of AMOLF, which is partly financed by the Dutch Research Council (NWO). The authors acknowledge funding from NWO under the KIC Key Technology CATLight project (grant number KICH1.ST01.20.021). The authors further acknowledge financial support from Holland High Tech (TKI HTSM) through the PPS Innovation scheme (project SHINER, 24PPS077). A large language model was used to assist with refining and editing the manuscript text. The original draft, all scientific content, analysis, and conclusions are the work of the authors.


### Conflicts of Interest

The authors declare no conflicts of interest.

### Data Availability Statement

The data that support the findings of this study are available from the corresponding author upon reasonable request.

### References


1. J. K. Nørskov, T. Bligaard, J. Rossmeisl, and C. H. Christensen, "Towards the Computational Design of Solid Catalysts," *Nature Chemistry* 1, no. 1 (2009): 37–46, https://doi.org/10.1038/nchem.121.

2. R. Ferrando, J. Jellinek, and R. L. Johnston, "Nanoalloys: From Theory to Applications of Alloy Clusters and Nanoparticles," *Chemical Reviews* 108, no. 3 (2008): 845–910, https://doi.org/10.1021/cr040090g.

3. J. Liu, P. Li, J. Bi, et al., "Switching Between C2+ Products and CH4 in CO2 Electrolysis by Tuning the Composition and Structure of Rare-Earth/Copper Catalysts," *Journal of the American Chemical Society* 145, no. 42 (2023): 23037–23047, https://doi.org/10.1021/jacs.3c05562.

4. C. Wu, H. Li, H. He, et al., "Compressive Strain in Core–Shell Au–Pd Nanoparticles Introduced by Lateral Confinement of Deformation Twinnings to Enhance the Oxidation Reduction Reaction Performance," *ACS Applied Materials and Interfaces* 11, no. 50 (2019): 46902–46911, https://doi.org/10.1021/acsami.9b16994.

5. S. Thota, Y. Wang, and J. Zhao, "Colloidal Au–Cu Alloy Nanoparticles: Synthesis, Optical Properties and Applications," *Materials Chemistry Frontiers* 2, no. 6 (2018): 1074–1089, https://doi.org/10.1039/c7qm00538e.

6. W. Zhan, J. Wang, H. Wang, et al., "Crystal Structural Effect of AuCu Alloy Nanoparticles on Catalytic CO Oxidation," *Journal of the American Chemical Society* 139, no. 26 (2017): 8846–8854, https://doi.org/10.1021/jacs.7b01784.

7. J. Yin, S. Shan, L. Yang, et al., "Gold–Copper Nanoparticles: Nanostructural Evolution and Bifunctional Catalytic Sites," *Chemistry of Materials* 24, no. 24 (2012): 4662–4674, https://doi.org/10.1021/cm302097c.

8. G. Guisbiers, S. Mejia-Rosales, S. Khanal, F. Ruiz-Zepeda, R. L. Whetten, and M. Jose-Yacaman, "Gold–Copper Nano-Alloy,"Tumbaga", in the Era of Nano: Phase Diagram and Segregation," *Nano Letters* 14, no. 11 (2014): 6718–6726, https://doi.org/10.1021/nl503584q.

9. N. E. Motl, E. Ewusi-Annan, I. T. Sines, L. Jensen, and R. E. Schaak, "AuCu Alloy Nanoparticles with Tunable Compositions and Plasmonic Properties: Experimental Determination of Composition and Correlation with Theory," *The Journal of Physical Chemistry C* 114, no. 45 (2010): 19263–19269, https://doi.org/10.1021/jp107637j.

10. M. Sun, A. Wang, M. Zhang, S. Zou, and H. Wang, "Interband and Intraband Hot Carrier-Driven Photocatalysis on Plasmonic Bimetallic Nanoparticles: A Case Study of Au–Cu Alloy Nanoparticles," *ACS Nanoscience Au* 4, no. 5 (2024): 360–373, https://doi.org/10.1021/acsnanoscienceau.4c00035.

11. H. Prunier, J. Nelayah, C. Ricolleau, et al., "New Insights into the Mixing of Gold and Copper in a Nanoparticle From a Structural Study of Au–Cu Nanoalloys Synthesized Via a Wet Chemistry Method and Pulsed Laser Deposition," *Physical Chemistry Chemical Physics* 17, no. 42 (2015): 28339–28346, https://doi.org/10.1039/c5cp01491c.

12. L. M. Vogl, P. Schweizer, X. Maeder, I. Utke, A. M. Minor, and J. Michler, "Unraveling Interdiffusion Phenomena and the Role of Nanoscale Diffusion Barriers in the Copper–Gold System," *ACS Nano* 18, no. 43 (2024): 29658–29666, https://doi.org/10.1021/acsnano.4c08502.

13. M. T. Candela, S. Triviño-Sánchez, A. Guerrero-Martínez, L. M. Liz-Marzán, and G. González-Rubio, "Pulsed Laser-Assisted Phase Engineering of Multimetallic Colloidal Nanocrystals With Complex Compositions," *Advanced Materials* (2026): e23683, https://doi.org/10.1002/adma.202523683.

14. Z. Swiatkowska-Warkocka, A. Pyatenko, F. Krok, B. R. Jany, and M. Marszalek, "Synthesis of New Metastable Nanoalloys of Immiscible Metals With a Pulse Laser Technique," *Scientific Reports* 5, no. 1 (2015): 9849, https://doi.org/10.1038/srep09849.

15. G. González-Rubio, P. Díaz-Núñez, W. Albrecht, et al., "Controlled Alloying of Au@Ag Core-Shell Nanorods Induced by Femtosecond Laser Irradiation," *Advanced Optical Materials* 9, no. 7 (2021): 2002134, https://doi.org/10.1002/adom.202002134.

16. A. Tymoczko, M. Kamp, O. Prymak, et al., "How the Crystal Structure and Phase Segregation of Au–Fe Alloy Nanoparticles are Ruled by the Molar Fraction and Size," *Nanoscale* 10, no. 35 (2018): 16434–16437, https://doi.org/10.1039/c8nr03962c.

17. A. Basagni, V. Torresan, P. Marzola, M. B. F. van Raap, L. Nodari, and V. Amendola, "Structural Evolution Under Physical and Chemical Stimuli of Metastable Au– Fe Nanoalloys Obtained by Laser Ablation in Liquid," *Faraday Discussions* 242 (2023): 286–300, https://doi.org/10.1039/d2fd00087c.

18. F. Waag, Y. Li, A. R. Ziefuß, et al., "Kinetically-Controlled Laser-Synthesis of Colloidal High-Entropy Alloy Nanoparticles," *RSC Advances* 9, no. 32 (2019): 18547–18558, https://doi.org/10.1039/c9ra03254a.

19. S. Triviño-Sánchez, R. Xu, J. González-Izquierdo, et al., "Colloidal Gold-Palladium-Platinum Alloy Nanospheres With Tunable Compositions and Defined Numbers of Atoms," *Nanoscale* 17, no. 14 (2025): 8577–8587, https://doi.org/10.1039/d4nr04898a.

20. A. Skorikov, W. Albrecht, E. Bladt, et al., "Quantitative 3D Characterization of Elemental Diffusion Dynamics in Individual Ag@Au Nanoparticles With Different Shapes," *ACS Nano* 13, no. 11 (2019): 13421–13429, https://doi.org/10.1021/acsnano.9b06848.

21. B. Barwick, H. S. Park, O.-H. Kwon, J. S. Baskin, and A. H. Zewail, "4D Imaging of Transient Structures and Morphologies in Ultrafast Electron Microscopy," *Science* 322, no. 5905 (2008): 1227–1231.

22. T. LaGrange, P. Cattaneo, B. Barwick, D. J. Flannigan, J. Weissenrieder, and F. Carbone, "Laser-Driven Ultrafast Transmission Electron Microscopy," *Nature Reviews Methods Primers* 5, no. 1 (2025): 61.





16136829, 0, Downloaded from https://onlinelibrary.wiley.com/doi/10.1002/smll.75977 by Centrum Voor Wiskunde En Info (Cwi), Wiley Online Library on [10/11/2026]. See the Terms and Conditions (https://onlinelibrary.wiley.com/terms-and-conditions) on Wiley Online Library for rules of use; OA articles are governed by the applicable Creative Commons License

23. A. M. Zak, "Light-Induced In Situ Transmission Electron Microscopy Development, Challenges, and Perspectives," *Nano Letters* 22, no. 23 (2022): 9219–9226, https://doi.org/10.1021/acs.nanolett.2c03669.

24. D. L. Jernigan and J. L. McAtee, "The Study of Carbon-Coated Grids at Elevated Temperatures by Electron Microscopy," *Thermochimica Acta* 4, no. 3 (1972): 393–404, https://doi.org/10.1016/0040-6031(72)87020-5.

25. Z. Zhang and D. Su, "Behaviour of TEM Metal Grids During In-Situ Heating Experiments," *Ultramicroscopy* 109, no. 6 (2009): 766–774, https://doi.org/10.1016/j.ultramic.2009.01.015.

26. A. R. Denton and N. W. Ashcroft, "Vegard's Law," *Physical Review A* 43 (1991): 3161–3164, https://doi.org/10.1103/PhysRevA.43.3161.

27. S. Y. Lee, N. Mettlach, N. Nguyen, Y. M. Sun, and J. M. White, "Copper Oxide Reduction Through Vacuum Annealing," *Applied Surface Science* 206, no. 1–4 (2003): 102–109.

28. B. Sundman, S. G. Fries, and W. A. Oates, "A Thermodynamic Assessment of the Au-Cu System," *Calphad* 22, no. 3 (1998): 335–354.

29. D. B. Butrymowicz, J. R. Manning, and M. E. Read, "Diffusion in Copper and Copper Alloys, Part II. Copper-Silver and Copper-Gold Systems," *Journal of Physical and Chemical Reference Data* 3, no. 2 (1974): 527–602.

30. B. Wu, D. Liu, S. Mubeen, T. T. Chuong, M. Moskovits, and G. D. Stucky, "Anisotropic Growth of TiO2 onto Gold Nanorods for Plasmon-Enhanced Hydrogen Production from Water Reduction," *Journal of the American Chemical Society* 138, no. 4 (2016): 1114–1117, https://doi.org/10.1021/jacs.5b11341.

31. C. Fang, H. Jia, S. Chang, et al., "(Gold core)/(Titania shell) Nanostructures For Plasmon-Enhanced Photon Harvesting and Generation of Reactive Oxygen Species," *Energy and Environmental Science* 7, no. 10 (2014): 3431–3438, https://doi.org/10.1039/C4EE01787K.

32. H. Al-Johani, E. Abou-Hamad, A. Jedidi, et al., "The Structure and Binding Mode of Citrate in the Stabilization of Gold Nanoparticles," *Nature Chemistry* 9, no. 9 (2017): 890–895, https://doi.org/10.1038/nchem.2752.

33. C. Ophus, "Four-Dimensional Scanning Transmission Electron Microscopy (4D-STEM): From Scanning Nanodiffraction to Ptychography and Beyond," *Microscopy and Microanalysis* 25, no. 3 (2019): 563–582, https://doi.org/10.1017/S1431927619000497.

34. F. de la Peña, E. Prestat, J. Lähnemann, et al., "hyperspy/hyperspy: v2.3.0, Zenodo," (Mar 2025), https://doi.org/10.5281/zenodo.14956374.

35. W. Van den Broek, A. Rosenauer, B. Goris, et al., "Correction of Non-Linear Thickness Effects in HAADF STEM Electron Tomography," *Ultramicroscopy* 116 (2012): 8–12, https://doi.org/10.1016/j.ultramic.2012.03.005.

36. W. van Aarle, W. J. Palenstijn, J. De Beenhouwer, et al., "The ASTRA Toolbox: A Platform For Advanced Algorithm Development in Electron Tomography," *Ultramicroscopy* 157 (2015): 35–47, https://doi.org/10.1016/j.ultramic.2015.05.002.

37. M. Dieperink, A. Skorikov, N. Claes, S. Bals, and W. Albrecht, "Considerations For Electromagnetic Simulations For a Quantitative Correlation of Optical Spectroscopy and Electron Tomography of Plasmonic Nanoparticles," *Nanophotonics* 13, no. 25 (2024): 4647–4665, https://doi.org/10.1515/nanoph-2024-0238.

## Supporting Information

Additional supporting information can be found online in the Supporting Information section.

**Supporting File 1**: smll75977-sup-0001-SuppMat.pdf.

**Supporting File 2**: smll75977-sup-0002-S1.mp4.



16136829, 0, Downloaded from https://onlinelibrary.wiley.com/doi/10.1002/smll.75977 by Centrum Voor Wiskunde En Info (Cwi), Wiley Online Library on [10/11/2026]. See the Terms and Conditions (https://onlinelibrary.wiley.com/terms-and-conditions) on Wiley Online Library for rules of use; OA articles are governed by the applicable Creative Commons License